

An updated efficient galaxy morphology classification model based on ConvNeXt encoding with UMAP dimensionality reduction

GUANWEN FANG ^{1,2,*} SHIWEI ZHU ^{1,2} JUN XU ^{1,2} SHIYING LU ^{1,2,3} CHICHUN ZHOU ⁴ YAO DAI ^{5,6} ZESEN LIN ⁷
AND XU KONG ^{8,9,10}

¹*School of Mathematics and Physics, Anqing Normal University, Anqing 246011, China; wen@mail.ustc.edu.cn*

²*Institute of Astronomy and Astrophysics, Anqing Normal University, Anqing 246133, China*

³*Key Laboratory of Modern Astronomy and Astrophysics (Nanjing University), Ministry of Education, Nanjing 210093, China*

⁴*School of Engineering, Dali University, Dali 671003, China*

⁵*Shanghai Astronomical Observatory, Chinese Academy of Sciences, 80 Nandan Road, Shanghai 200030, China*

⁶*School of Astronomy and Space Science, University of Chinese Academy of Sciences, No. 19A Yuquan Road, Beijing 100049, China*

⁷*Institute for Astrophysics, School of Physics, Zhengzhou University, Zhengzhou, 450001, China*

⁸*Department of Astronomy, University of Science and Technology of China, Hefei 230026, China; xkong@ustc.edu.cn*

⁹*School of Astronomy and Space Science, University of Science and Technology of China, Hefei 230026, China*

¹⁰*Institute of Deep Space Sciences, Deep Space Exploration Laboratory, Hefei 230026, China*

ABSTRACT

We present an enhanced unsupervised machine learning (UML) module within our previous USmorph classification framework featuring two components: (1) hierarchical feature extraction via a pre-trained ConvNeXt convolutional neural network (CNN) with transfer learning, and (2) nonlinear manifold learning using Uniform Manifold Approximation and Projection (UMAP) for topology-aware dimensionality reduction. This dual-stage design enables efficient knowledge transfer from large-scale visual datasets while preserving morphological pattern geometry through UMAP's neighborhood preservation. We apply the upgraded UML on I-band images of 99,806 COSMOS galaxies at redshift $0.2 < z < 1.2$ (to ensure rest-frame optical morphology) with $I_{\text{mag}} < 25$. The predefined cluster number is optimized to 20 (reduced from 50 in the original framework), achieving significant computational savings. The 20 algorithmically identified clusters are merged into five physical morphology types. About 51% of galaxies (50,056) were successfully classified. To assess classification effectiveness, we tested morphological parameters for massive galaxies with $M_* > 10^9 M_\odot$. Our classification results align well with galaxy evolution theory. This improved algorithm significantly enhances galaxy morphology classification efficiency, making it suitable for large-scale sky surveys such as those planned with the China Space Station Telescope (CSST).

Keywords: Galaxy structure (622), Astrostatistics techniques (1886), Astronomy data analysis (1858)

1. INTRODUCTION

The morphology and structure observed in galaxy images are capable of revealing numerous physical properties, including color, gas content, star formation rate, stellar mass, and environment (e.g., Kauffmann et al. 2004; Omand et al. 2014; Kawinwanichakij et al. 2017; Siudek et al. 2022; Huertas-Company et al. 2024; Ghosh et al. 2024; Su et al. 2025). With the rapid development of astronomical observation technologies and the implementation of numerous large-scale sky surveys, an enormous amount of astronomical data has been generated (e.g., Stoughton et al. 2002; Scoville et al. 2007). Consequently, conventional expert visual inspection (Hubble 1926; Flügge 1959) methods have become inadequate for processing such data. Machine learning (ML), owing to its robust

data processing capabilities, has emerged as a critical tool in astronomy.

Machine learning (ML) is commonly categorized into two main types: supervised machine learning (SML) and unsupervised machine learning (UML). The former one (i.e., SML), such as convolutional neural networks (CNNs; Lecun et al. 1998), through pretraining, can learn hierarchical features from images, enabling detailed classification of galactic fine-scale structures such as bulges, disks, spiral arms, and bars (e.g., Simmons et al. 2014; Davis & Hayes 2014; Dieleman et al. 2015; Fernando et al. 2024). For instance, Huertas-Company et al. (2015) trained a five-layer CNN using visual classification data from approximately 8,000 H-band galaxies in the CANDELS fields. However, SML requires training with large annotated datasets, and constructing such high-quality annotated datasets often incurs substantial time and resource consumption.

* Corresponding author: Guanwen Fang

Recent studies have shown that transfer learning and domain adaptation can partly alleviate this requirement by adapting pretrained models to new surveys with only a modest number of labelled targets (e.g., Domínguez Sánchez et al. 2019; Ćiprijanović et al. 2023). Nevertheless, these methods still rely on some labelled data, and their performance is sensitive to domain shifts such as Point Spread Function (PSF), depth, and redshift, which limits their general applicability. As a result, the latter one (i.e., UML) is widely employed to analyze large-scale unlabeled datasets for classification and annotation. UML can not only extract features from raw images but also cluster galaxies in terms of similar features (e.g., Cheng et al. 2021; Kolesnikov et al. 2023). For example, Cheng et al. (2021) employed a Vector-Quantized Variational Autoencoder (VQ-VAE) combined with hierarchical clustering algorithms to extract features and classify galaxy images from the Sloan Digital Sky Survey (SDSS; York et al. 2000), successfully categorizing galaxies into 27 distinct groups characterized by varying morphological features and physical properties. The Self-supervised learning (SSL; Gui et al. 2024) is generally regarded as a branch of UML, as it learns feature representations from unlabeled data through automatically generated supervision signals rather than manual annotations. For instance, the vision transformer (ViT; Dosovitskiy et al. 2021) effectively extracts features from similar data domains. Meanwhile, contrastive learning frameworks (e.g., Chen et al. 2020; Grill et al. 2020) learn feature representations by constructing positive and negative sample pairs, obviating the need for explicit data labels.

However, the effectiveness of UML methods strongly depends on the quality of the learned feature representations. In high-dimensional fields, such as image data, the structural complexity of features is pronounced, accompanied by significant noise and redundant information. This phenomenon complicates the ability of unsupervised models to identify key feature dimensions, leading to notable degradation in tasks such as feature extraction and cluster analysis (e.g., Zhou et al. 2022; Jang & Tong 2024). To address the computational and performance limitations of UML in high-dimensional data, dimensionality reduction techniques, such as principal component analysis (PCA; Maćkiewicz & Ratajczak 1993), t-distributed stochastic neighbor embedding (t-SNE; van der Maaten & Hinton 2008), and uniform manifold approximation and projection (UMAP; McInnes & Healy 2018), have been increasingly integrated into UML frameworks. For example, PCA identifies principal components with maximal variance through linear transformation, discarding components with negligible variance contributions. This process preserves dominant data features while eliminating redundant information, offering two key advantages: (1) substantial reduction in computational resource requirements, and (2) acceleration of downstream analytical tasks via optimized data representations. This synergistic approach effectively balances dimensionality reduction and information retention, addressing both computational efficiency and analytical performance in UML applications.

In our prior research, Zhou et al. (2022) developed our initial galaxy morphology classification framework, i.e., the Bagging-based voting clustering approach. By integrating Convolutional Autoencoders (CAE; Masci et al. 2011) to reduce image noise effectively, this method successfully clustered galaxies into 100 groups with high intra-group similarity. Then, Fang et al. (2023) introduced the Adaptive Polar Coordinate Transformation (APCT) technique, which can improve rotational invariance during image processing, enhancing model robustness and demonstrating GoogLeNet’s superior performance in galaxy classification. Subsequently, Dai et al. (2023) first systematically combined UML and SML methods to classify 17,292 galaxies in the COSMOS-DASH field. Building on the study of Dai et al. (2023), Song et al. (2024) proposed the US_{morph} model, which was the same hybrid framework (i.e., UML plus SML) as that in Dai et al. (2023) but with a self-consistent data pre-processing pipeline, to cluster the galaxy images into 50 groups successfully. This study expanded the dataset sixfold, classified nearly 100,000 galaxies in the COSMOS field, and validated the model’s efficiency and reliability in large-scale classification tasks.

In this work, we introduce an unsupervised clustering algorithm that integrates pre-trained large-scale encoder models with dimensionality reduction techniques. The methodology optimizes computational resource utilization through latent space compression and simplifies feature representations, enabling efficient and streamlined unsupervised clustering. Based upon the US_{morph} framework (Song et al. 2024), we propose two methodological advancements implemented immediately following pre-processing steps: (1) we utilize a pretrained ConvNeXt model (Liu et al. 2022) to extract hierarchical image features; (2) we perform subsequent feature refinement via Uniform Manifold Approximation and Projection (UMAP, McInnes & Healy 2018), achieving effective dimensionality reduction. The data pre-processing employs a CAE (Masci et al. 2011) combined with APCT (Fang et al. 2023). This step aims to mitigate the effects of noise and enhance rotational invariance in image features. Subsequently, the ConvNeXt model is applied to perform deep encoding of preprocessed images, extracting discriminative features. The encoded features undergo dimensionality reduction via the UMAP algorithm, where nonlinear manifold learning further optimizes feature representations. This dual strategy of deep feature extraction and dimensionality reduction is designed to maximize the extraction of critical data features and eliminate redundant dimensions, enabling efficient compression of the feature space. This not only improves downstream task performance but also significantly reduces computational resource consumption and storage requirements. Finally, a Bagging-based voting clustering model (Zhou et al. 2022) is implemented to classify the refined features. We optimize the UML’s predefined cluster number to 20 (reduced from 50 in the original US_{morph} framework of Song et al. (2024)), and achieve significant computational savings. The machine recognized 20 pre-stage groups, which were then converged to five physical morphology types. UMAP (McInnes & Healy 2018) data visualization and analysis of galaxy morphology

parameter distributions are conducted to verify the reliability of the classification results.

The structure of this paper is as follows. Section 2 provides an overview of the COSMOS program and sample selection criteria. Section 3 introduces the improved unsupervised galaxy morphology classification model, as well as the application of UMAP technology. Section 4 presents classification results and system parameter measurements. Section 5 summarizes the main conclusions and provides an outlook for future research. Throughout this paper, we use the AB magnitude system (Oke & Gunn 1983) and assume a Chabrier (2003) initial mass function and a standard flat Λ CDM cosmology with parameters $H_0 = 70 \text{ km s}^{-1} \text{ Mpc}^{-1}$, $\Omega_m = 0.3$, and $\Omega_\Lambda = 0.7$.

2. OBSERVATION AND SAMPLE SELECTION

The COSMOS survey (Scoville et al. 2007) is a large observational program dedicated to studying galaxy evolution, star formation, active galactic nuclei, and the relationship between dark matter and large-scale structure within the redshift range $0.5 < z < 6$. It covers an area of approximately 2 deg^2 and employs multi-wavelength imaging and spectroscopic observations spanning from X-ray to radio. This survey includes high-resolution imaging data from the Hubble Space Telescope (HST) using the Advanced Camera for Surveys (ACS) in the F814W filter, which covers the largest contiguous area ($\sim 1.64 \text{ deg}^2$) within the COSMOS region. The original image collection comprises approximately 590 pointings, with an average exposure time of 2028 seconds per pointing. The original images were processed by Koekemoer et al. (2007) using the MultiDrizzle package (Koekemoer et al. 2003). The final mosaic images have a pixel scale of $0''.03$ and a 5σ depth of 27.2 AB magnitude for point-source observations within an aperture diameter of $0''.24$. Subsequent analyses in this study are based on these high-resolution mosaic images.

The dataset used in this study is from the ‘‘Farmer’’ COSMOS2020 catalog (Weaver et al. 2022), which provides comprehensive photometric data across 35 bands spanning from ultraviolet to mid-infrared wavelengths. The catalog was generated by modeling and performing photometric measurements on multi-band images using the Tractor package (Lang et al. 2016). Thus, many physical properties can be derived by fitting the spectral energy distribution (SED) of galaxies, including redshifts, stellar masses, and other parameters. For the determination of photometric redshifts, Weaver et al. (2022) utilized two distinct codes: EAZY (Brammer et al. 2008) and LePhare (Ilbert et al. 2008). The redshift estimation process in LePhare involved a library composed of 33 galactic templates. A detailed comparison demonstrated high consistency between the two methods in calculating photometric redshifts. In this work, we adopted the redshifts obtained from LePhare, as shown in Figure 15 of Weaver et al. (2022).

Based on the COSMOS2020 catalog, we selected the parent sample of galaxies by below criteria: (1) $l_{\text{type}} = 0$, to ensure that we select galaxies rather than stars; (2) $\text{FLAG}_{\text{COMBINE}} = 0$, to make sure that flux measurements

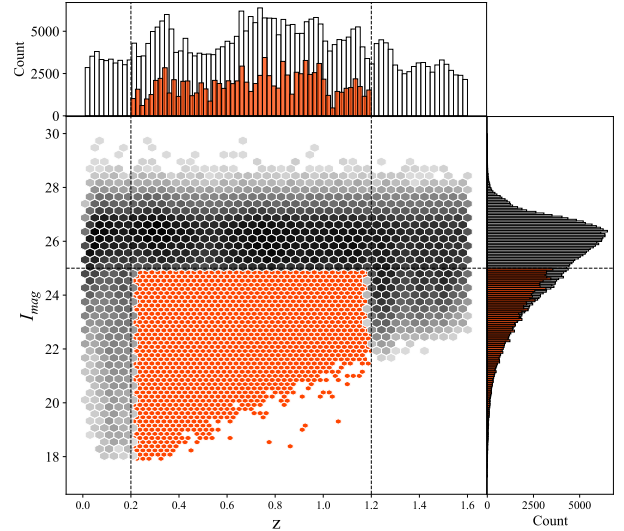


Figure 1. Distribution of galaxies in the COSMOS field in the I-band magnitude-redshift plane. The corresponding number distributions along I_{mag} and redshift are displayed at the top and right corners, respectively. The sample of galaxies at $0.2 < z < 1.2$ with $I_{\text{mag}} < 25$ is shown in orange.

are unaffected by the bright stars and that the objects are not at the image edges, which can guarantee reliable measurements on redshifts and stellar mass; (3) $0.2 < z < 1.2$, to ensure the galaxy morphologies measured in the rest-frame optical; (4) the high quality of source images with the signal-to-noise ratio (S/N) larger than 5 and without anomalous pixels. As a result, there are 99,806 galaxies retained. Figure 1 illustrates the distribution of galaxies between I-band magnitude and redshift in the COSMOS field, where the parent sample is shown in orange, satisfying $0.2 < z < 1.2$ and $I_{\text{mag}} < 25$.

3. METHOD FOR MORPHOLOGICAL CLASSIFICATION

In this section, we present the framework of the updated UML technology, which is structured into four primary components, including data pre-processing, feature extraction, UMAP dimensionality reduction, and voting based on a Bagging clustering model.

3.1. Data pre-processing

During the data pre-processing stage, we uniformly cropped all images to 100×100 pixels to ensure that sufficient structural information is preserved. As we find that the cropped size is related to the effective radii of galaxies in our sample, we adopt the GALAPAGOS software (Barden et al. 2012; Häußler et al. 2022) to measure the effective radius of each galaxy. The following statistical analysis reveals that 98% of the sample galaxies have effective radii smaller than 50 pixels, suggesting that the adopted pixel size (i.e., 100×100 pixels) used to crop images is enough to support subsequent morphological classification tasks.

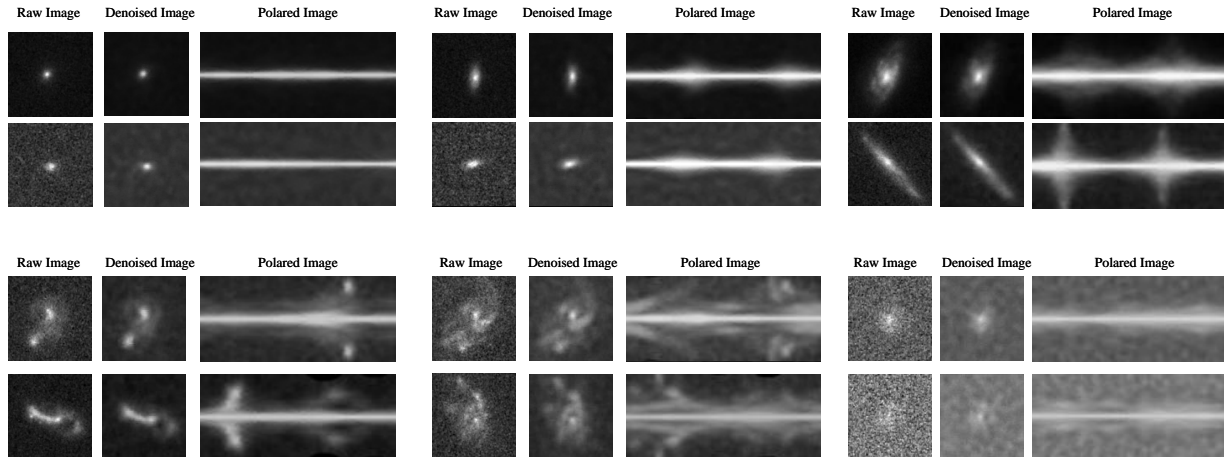


Figure 2. Six examples of the image pre-processing flow, corresponding to each set of images from left to right: original image, denoised image, and image after the polar coordinate transformation.

To enhance the model’s classification stability, we incorporate data pre-processing steps. In response to the adverse effects of high noise levels – resulting from low S/N – on galaxy classification accuracy, we apply CAE for image denoising. During CAE processing, convolutional and pooling operations automatically extracted key features, which were then used to reconstruct denoised images while preserving essential structural information intact. Table 1 lists the architecture and layer parameters of the CAE employed in this study. As shown in Figure 2, the left column of each sample image set represents the original data, and the middle column displays the CAE-denoised reconstructed images. This process effectively removes noise and artifacts from the images while successfully retaining the fundamental morphological features of the galaxies.

In galaxy morphology classification, spatial rotations can lead to misclassification of morphological types. To eliminate rotational interference and achieve rotation-invariant feature extraction, we implement the APCT technique proposed by Fang et al. (2023) to enhance the model robustness by constructing a rotation-invariant feature space. The workflow of this method involves three steps. First, an initial polar axis should be defined by connecting extremum brightness points (maximum/minimum pixel values) in the image. Subsequently, the polar axis needs to be rotated counterclockwise in increments of 0.05 radian, where pixels along the rotational polar axis are aggregated into polar coordinates via a stacking process. Finally, we apply mirror transformations to accentuate central features.

By employing an APCT, image rotations are converted into translations in the polar coordinate system, thereby transforming the inherent translation invariance of CNNs into rotation invariance. As demonstrated by Fang et al. (2023), APCT maintains classification accuracy at a level comparable to unrotated images even under large rotations (90° – 270°), whereas models without APCT suffer a substantial performance drop. This clearly highlights its effectiveness in improving orienta-

Table 1. The CAE architecture illustration

Layer	Operation	Dimension	Filter Size	Stride
L0	Input	$100 \times 100 \times 1$
L1	Convolution	$100 \times 100 \times 8$	5×5	...
L2	Maxpooling	$50 \times 50 \times 8$	2×2	2×2
L3	Convolution	$50 \times 50 \times 8$	5×5	...
L4	Maxpooling	$25 \times 25 \times 8$	2×2	2×2
L5	Unfolding	10000
L6	Full connection	40

Note: The CAE employs a symmetric encoder-decoder architecture. The encoder processes a 100×100 pixel input through two convolutional layers. The first layer has 16 channels with 5×5 kernels and max-pooling (2×2 kernel, stride 2). The second layer uses 8 filters and max-pooling (2×2 kernel, stride 2), resulting in $25 \times 25 \times 16$ feature maps. These are flattened and passed through a fully connected layer to produce a 40-dimensional latent space. The decoder reconstructs the output using unpooling and deconvolution to mirror the encoder structure.

tion invariance. Compared with conventional rotation-based data augmentation (e.g., Reyes et al. 2018; Yao et al. 2019), APCT achieves rotation invariance more efficiently, thereby reducing the computational burden in large-scale sky survey analyses. Furthermore, APCT processing accentuates feature contrasts and improves label alignment, leading to further gains in classification accuracy. The right panel of each image set in Figure 2 displays the corresponding results after APCT implementation.

3.2. ConvNeXt model framework and feature extraction

In recent years, deep visual models have shown remarkable capability in learning hierarchical representations from large-scale datasets (e.g., Krizhevsky et al. 2012). Pre-trained architectures can serve as powerful feature extractors, enabling the

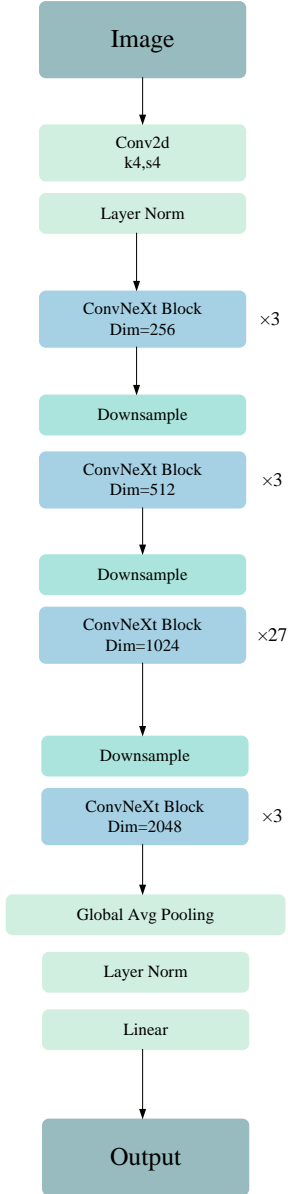


Figure 3. Framework of ConvNeXt model. The architecture of ConvNeXt employs a Transformer-inspired modular design, which hierarchically stacks standardized modules in a multi-level architecture. Inter-module communication and gradient propagation are facilitated via consistent architectural interfaces, ensuring efficient information flow and stable training dynamics. This design paradigm maintains structural simplicity while enhancing scalability, enabling systematic network expansion via modular composition.

extraction of transferable representations directly from unlabeled data. These models can effectively extract discriminative features without requiring labels for unlabeled data. ConvNeXt (Liu et al. 2022) is an efficient visual architecture. It enhances the ResNet framework (He et al. 2015) by introducing a patchify layer and adopting depthwise grouped convolutions to widen the network. This design merges the strengths of

CNNs and Swin Transformer (Dosovitskiy et al. 2021), leveraging CNNs’ robust local feature extraction while modeling long-range dependencies through self-attention mechanisms. Consequently, ConvNeXt demonstrates superior performance in image classification tasks (e.g., Woo et al. 2023; Liu et al. 2023). We utilize the ConvNeXt-22k model pre-trained on the ImageNet-22k dataset (Russakovsky et al. 2015). The architecture begins with an initial convolutional layer using a 4×4 kernel and a stride of 4, followed by LayerNorm for normalization. The model comprises multiple stages of ConvNeXt Blocks, which integrate depthwise separable convolutions, LayerNorm, GELU activation, and residual connections to facilitate effective feature extraction and information retention. These blocks are organized into groups with progressively increasing channel dimensions (256, 512, 1024, 2048), interspersed with downsampling layers to adjust spatial resolution. The network concludes with global average pooling, LayerNorm, and a linear classification layer (see Figure 3).

The ConvNeXt model employs depthwise separable convolutions to construct a lightweight architecture while enabling multi-scale feature extraction. The polarized image obtained after data processing is input into the ConvNeXt model for feature extraction, and galaxy images are transformed into 2048-dimensional feature vectors e , which efficiently filter out redundant information present in the original imagery, as illustrated in the corresponding step of Figure 4.

3.3. UMAP dimensionality reduction

To further extract key features, we employ dimensionality reduction techniques to compress the 2048-dimensional feature vectors output by the ConvNeXt model, optimizing the feature space while preserving essential information. Among traditional linear dimensionality reduction methods, PCA achieves dimensionality reduction by identifying orthogonal directions of maximal variance in high-dimensional data (principal components), maintaining the global linear structure. However, its linear nature imposes significant limitations when handling nonlinear manifold structures: when data distributions exhibit complex nonlinear patterns, PCA fails to effectively capture nonlinear relationships among data points and retains the local structure of nonlinear data poorly, necessitating the retention of excessive principal components to maintain information integrity, thereby drastically reducing reduction efficiency (e.g., McInnes & Healy 2018; Gong et al. 2018; Liu et al. 2023).

For high-dimensional data such as images, which often exhibit nonlinear manifold structures, the feature vectors extracted by pretrained encoders typically reside on a low-dimensional manifold (e.g., Mao et al. 2024; Lowe et al. 2024). As a nonlinear method rooted in manifold learning and topological principles, UMAP approximates the underlying manifold structure of data and preserves its topological relationships, enabling more precise revelation of intrinsic geometric features. Compared with linear dimensionality reduction algorithms, UMAP achieves significant dimensionality reduction while effectively balancing global and local structures and maintaining high information integrity, particularly excelling

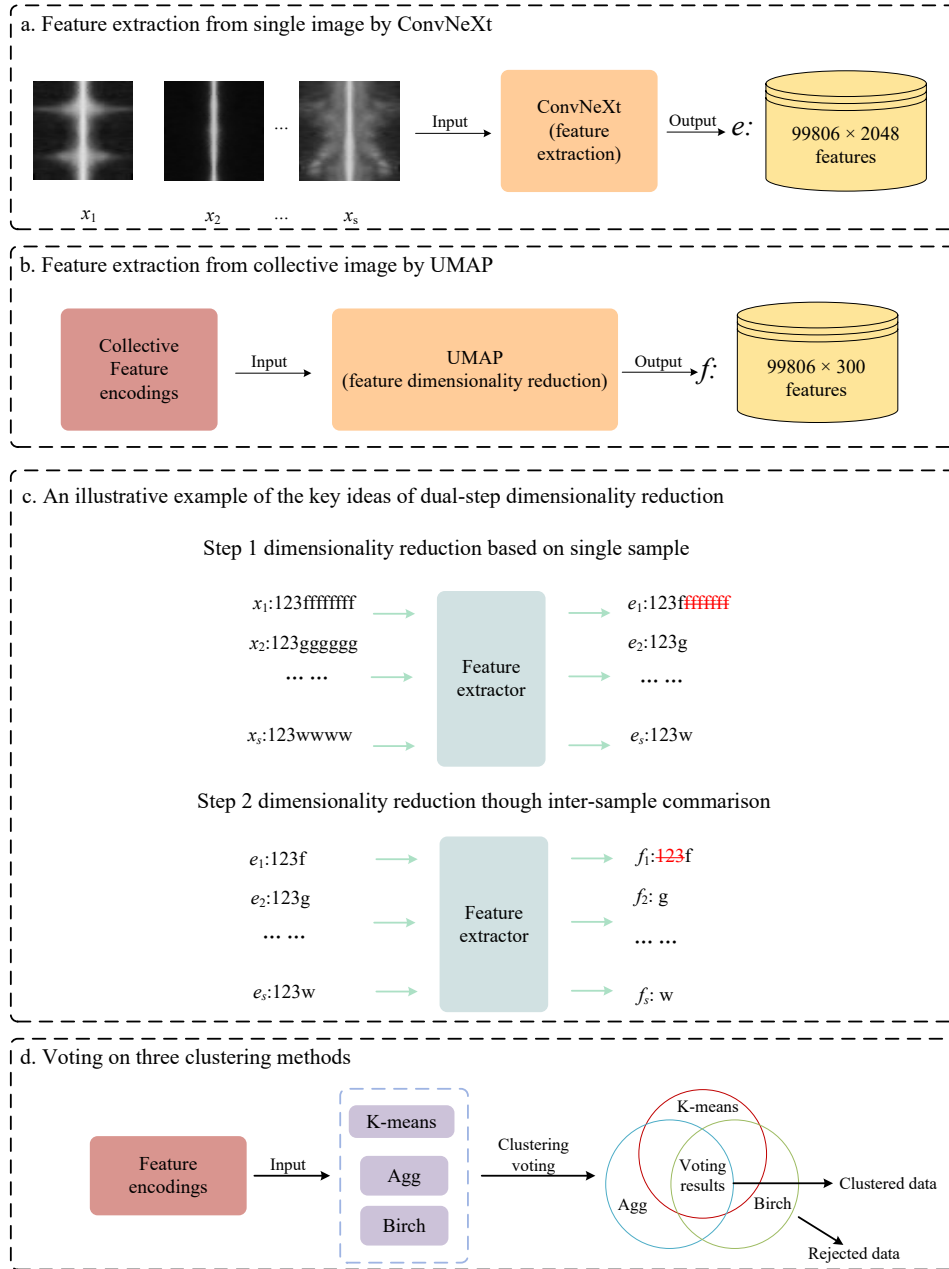


Figure 4. Schematic diagram of UML clustering process, including to extract key features from image data using ConvNeXt in step (a); to reduce dimensionality and remove redundant image information via UMAP in step (b); to provide a detailed example of the feature extraction and dimensionality reduction process in step (c); and to adopt a voting based on Bagging clustering model mechanism in step (d).

in handling high-dimensional data with complex nonlinear distributions, such as images. Specifically, UMAP’s dimensionality reduction process comprises three key steps: a) quantifying local similarities between each high-dimensional data point and its neighborhood points using an exponential probability distribution; b) strategically constructing a minimum spanning tree from these high-similarity connections to capture the global topological structure of the data manifold; c) employing stochastic gradient descent optimization to iteratively refine the low-dimensional embedding space by minimizing the cross-entropy loss between high-dimensional and low-

dimensional topological representations. Despite the complexity of its topological construction and optimization procedures, UMAP systematically reduces the computational complexity of key steps to near-linear levels. This is achieved through the integration of approximate nearest neighbor search, sparse graph representations, and optimization strategies that avoid global normalization (McInnes & Healy 2018). Consequently, UMAP achieves significantly higher efficiency compared to other nonlinear dimensionality reduction algorithms, making it well-suited for processing future large-scale sky survey data. This process systematically reduces discrepancies between

high-dimensional and low-dimensional topological characterizations, thereby achieving efficient dimensionality reduction while preserving the essential features of the data.

In nonlinear dimensionality reduction tasks, the selection of the low-dimensional space dimensionality in UMAP impacts algorithmic performance. Unlike linear methods such as PCA, which can determine optimal dimensionality through variance explained ratio calculations using the “elbow method”, UMAP primarily aims to preserve both local and global geometric structures of data rather than adhering to variance maximization principles. This necessitates manual specification of target dimensionality during the reduction process. Current research predominantly relies on empirical approaches or downstream task performance evaluation to select the dimension, which is highly subjective and computationally expensive (e.g., Liu et al. 2023; Zhu-Ge et al. 2023). Consequently, the development of appropriate dimensionality selection strategies becomes crucial for enhancing dimensionality reduction efficacy.

The Davies-Bouldin Index (DB Index; Davies & Bouldin 1979) is an internal metric for evaluating clustering quality. As an unsupervised measure, it operates independently of external information and assesses the validity of clustering results by quantifying the ratio between intra-cluster compactness and inter-cluster separation. The DB Index can be expressed as:

$$DB = \frac{1}{N} \sum_{i=1}^N \max_{j \neq i} \left(\frac{S_i + S_j}{d(c_i, c_j)} \right); \quad (1)$$

where S_i and S_j are the cohesiveness of cluster i and cluster j , respectively, defined as the average distance from the data points within the cluster to the cluster center. $d(c_i, c_j)$ represents the distance between the centers of cluster i and cluster j . N is the number of clusters, and c_i and c_j are the centers of the clusters. The DB index has a significant advantage in handling convex-shaped clusters (Halkidi et al. 2001). The smaller the index value, the better the clustering performance. To achieve a balance between effectiveness and efficiency in the UMAP dimensionality reduction process, we compute the DB index across dimensionality values ranging from 50 to 500 in increments of 50. The results show that the DB index reaches its minimum value at 300 dimensions. Consequently, we select 300 dimensions as the optimal output for dimensionality reduction. When determining the target dimensionality, the DB index is computed based on the clustering result from K-means. The calculation inherently leverages the cluster centroids to quantify intra-cluster dispersion and inter-cluster separation. This evaluation was performed with the number of clusters fixed at $k = 20$. For a comprehensive explanation of the clustering methodology and the rationale behind the choice of cluster count, please refer to Section 3.4.

As illustrated in Figure 4, after applying UMAP for dimensionality reduction, each galaxy image x is compressed from its original 2048-dimensional representation e (see panel a) to a 300-dimensional representation f (see panel b). In the two-step feature extraction process (see panel c), the first step

removes redundant features inherent in the data, retaining only the valid features. The second step further eliminates redundant features by comparing the differences between samples, and highlights key features.

3.4. UML Clustering Process

After data pre-processing, feature extraction, and UMAP dimensionality reduction, We employ a bagging-based multi-model voting classification method (Zhou et al. 2022) to improve classification reliability. This approach can remove sources with inconsistent cluster memberships across different algorithms. In this process, we use three algorithms to perform clustering voting: the Hierarchical Balanced Iterative Reduction and Clustering Algorithm (Birch; Zhang et al. 1996), the K-means Clustering Algorithm (K-means; Hartigan & Wong 1979), and the Agglomerative Clustering algorithm (Agg; Murtagh 1983; Murtagh & Legendre 2014). Each algorithm processes the data independently by partitioning the sample into 20 groups. We use the labels generated by the K-means algorithm as the reference labels, assign the corresponding labels to the other clustering models by counting the frequency of distribution of K-means labels within each group, and synchronize the majority voting mechanism. When the voting results of the three algorithms are identical, the samples that they contain together will be determined as the final sample set, and the rest of the samples that are not included in this set will be excluded. The clustering process refers to Step d in Figure 4.

In unsupervised clustering, the number of clusters k is typically set to a relatively high value based on the scientific objectives. A small k may fail to capture subtle differences in the data, resulting in overly coarse groupings, whereas an excessively large k can lead to overfitting, amplify noise, increase computational cost, and produce unstable results. Specifically, a low k (e.g., $k = 5$) fails to resolve key morphological classes, potentially causing galaxies to be grouped by non-morphological features such as S/N, while a high k (e.g., $k = 50$) produces redundant clusters, increasing computational load and drastically reducing the efficiency of subsequent visual inspection and labeling. To balance performance and efficiency, we adopt $k = 20$ as our clustering number. This choice effectively groups galaxy images with similar features while avoiding an excessive burden for subsequent manual labeling, thereby achieving a trade-off between classification accuracy and operational efficiency.

Based on the 300-dimensional feature representation obtained through UMAP dimensionality reduction, clustering was performed using a Bagging-based approach. After excluding 49,750 samples (49%) with inconsistent votes, a total of 50,056 galaxies were successfully classified into 20 distinct groups. To further analyze group classifications and assess differences in physical properties, a visual classification process was conducted. For this purpose, 100 images were randomly selected from each group, and three trained experts participated in the visual inspection step to minimize subjective bias. Final classifications were assigned only when at least two experts reached agreement. Consistent with our over-clustering

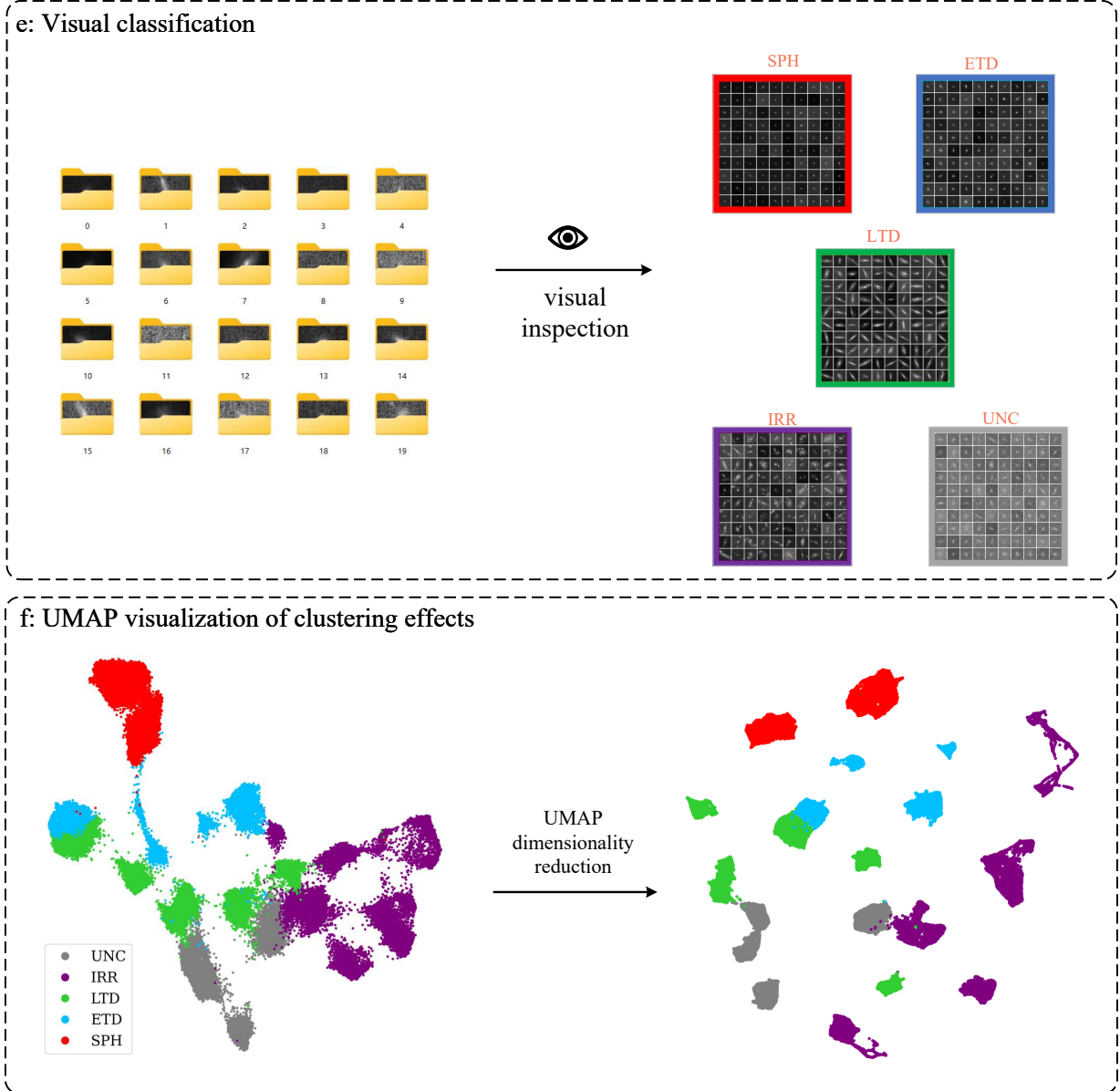


Figure 5. The continued schematic diagram of the UML clustering process as in Figure 4. Step (e) displays the Visual classification by randomly selecting 100 images from the 20 machine-learning clusters and visually classifying them into five types of galaxies, including SPH (spherical), ETD (early-type disk), LTD (late-type disk), IRR (irregular), and UNC (unclassified), respectively. Step (f) shows the UMAP visualization of clustering effects by analyzing the UMAP 2D projection of the five-class labels derived from the previous step. On the left, visualize the 2048-dimensional features of all samples extracted by the ConvNeXt model using UMAP; on the right, visualize the distribution of 300-dimensional features after UMAP-based dimensionality reduction.

strategy, the majority of galaxies within each group display highly similar morphological features. Empirically, more than 80% of the galaxies in each cluster were found to be morphologically homogeneous, which ensured that the 100 randomly inspected images provided a representative characterization of the entire cluster. This workflow is illustrated in Step e of Figure 5. Ultimately, these 50,056 galaxies were categorized into five morphological classes: spherical (SPH), early-type disk (ETD), late-type disk (LTD), irregular (IRR), and unclas-

Table 2. Number of galaxies in different morphological types

Model	SPH	ETD	LTD	IRR	UNC	TOTAL
UML	8,506	7,348	11,473	14,044	8,685	50,056

sified (UNC). The distribution of the number of galaxies in each category is detailed in Table 2.

4. RESULTS AND DISCUSSION

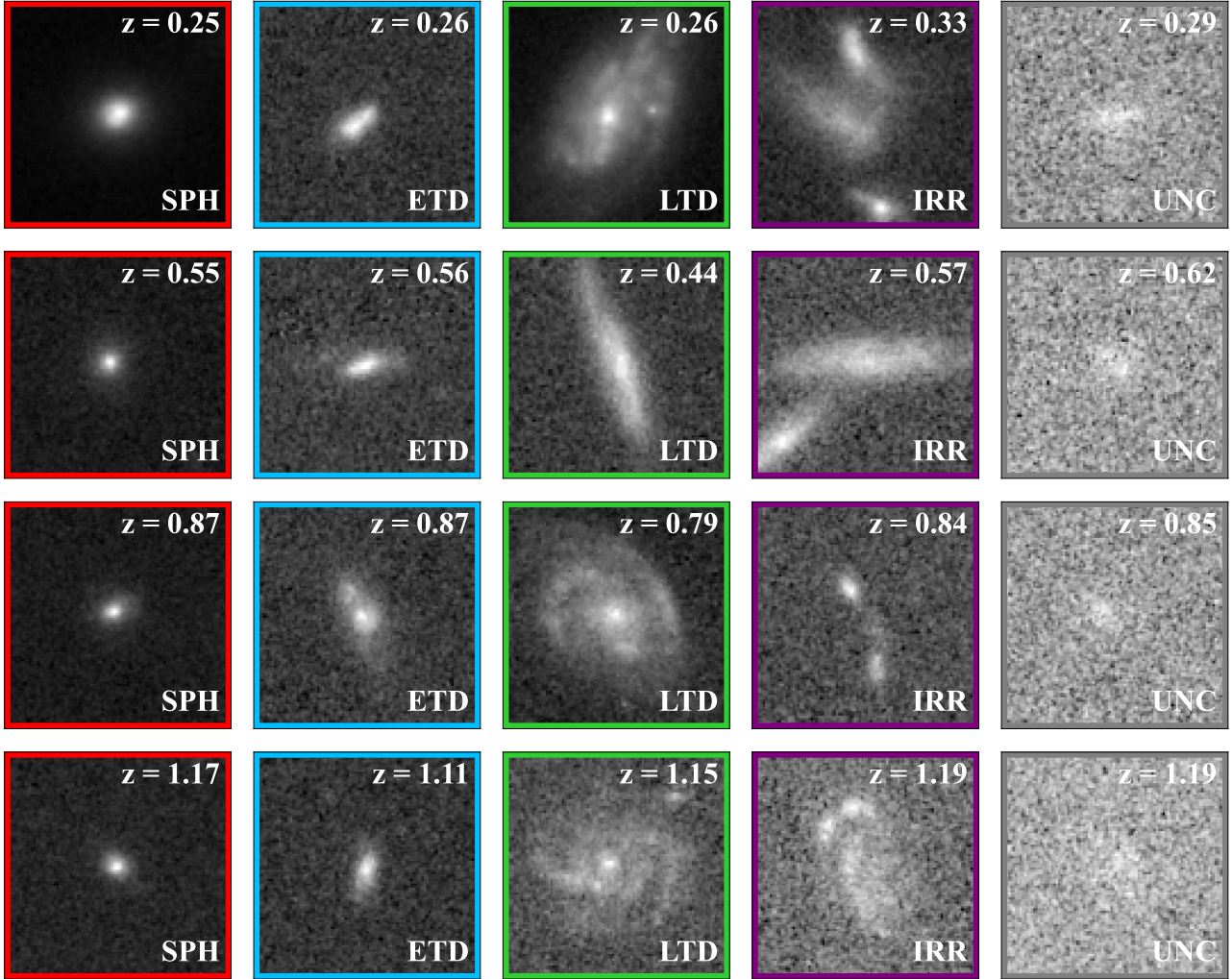


Figure 6. Example images of galaxies randomly selected from the sample. From left to right, images in each column correspond to spherical galaxies (SPHs), early-type disk galaxies (ETDs), late-type disk galaxies (LTDs), irregular galaxies (IRRs), and unclassified galaxies (UNCs), respectively.

4.1. Overall morphological classification results

Notably, UMAP (McInnes & Healy 2018) is not only widely applied in dimensionality reduction and clustering tasks but also frequently used for visual inspection of high-dimensional data. This algorithm efficiently maps high-dimensional complex data to a low-dimensional space (e.g., 2D or 3D) while preserving both local similarities and global structural characteristics. Thus, we utilize UMAP to project the 50,056 galaxy datasets into a 2D plane for intuitive visualization and analysis.

As shown in step f of Figure 5, the 2048-dimensional feature vectors extracted by the ConvNeXt model exhibit non-convex distribution characteristics due to their high dimensionality. After UMAP dimensionality reduction, the data becomes to exhibit convex clusters, with 90% of galaxy samples showing no overlap in the projection and clear boundaries between galaxy groups. Through updated UML technology, we have successfully classified 50,056 galaxies (51%) in the COS-

MOS field. This includes 8,506 SPHs, 7,348 ETDs, 11,473 LTDs, 14,044 IRRs, and 8,685 UNC. Figure 6 shows sample images of some galaxies. Intuitive comparisons reveal distinct differences between them.

4.2. Validation through Comparison with External Morphology Catalogs

To assess the scientific reliability of our enhanced UML-based automated classification method, we compare its results with those from Galaxy Zoo:Hubble (GZH; Willett et al. 2017). The GZH project, which relies on visual classifications by volunteers, adopts a classification framework centered on three principal structural types: SPH, DISK, and IRR. It produces a set of probabilistic morphological features, such as smoothness and the presence of structures or clumps, and develops a scalable automated classifier through statistical learning techniques. Since the GZH project offer adjustable thresholds to balance sample completeness and classification confidence, combined with HST/ACS F814W data from the

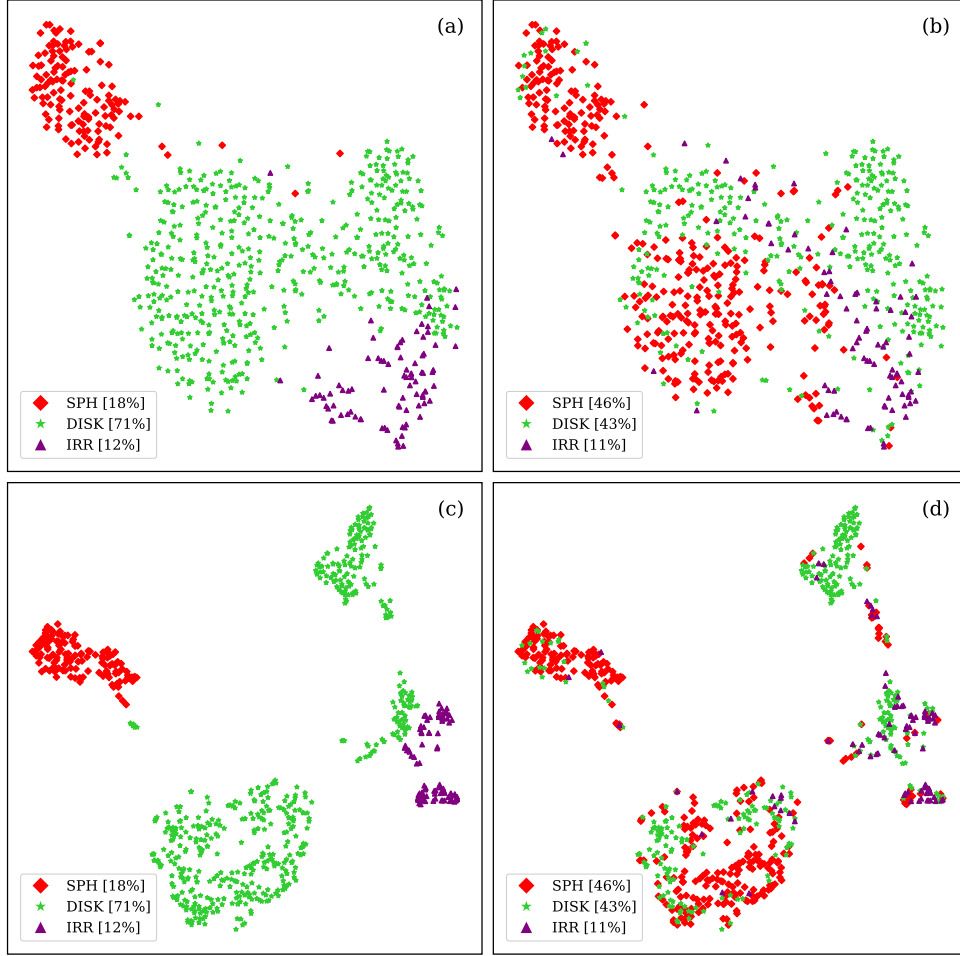


Figure 7. Two-dimensional visualization of morphological classification results for the matched subsample. Panel (a) depicts the t-SNE projection of the proposed UML method on ConvNeXt features (2048-dimensional), while Panel (b) presents the corresponding results from the Galaxy Zoo: Hubble catalog (Willett et al. 2017) on the same features. Panels (c) and (d) display t-SNE projections of the two methods on 300-dimensional features, respectively. Comparative analysis demonstrates that the proposed UML method (Panels a and c) exhibits more compact intra-class clustering and more distinct inter-class separation.

COSMOS field, it can serve as a suitable reference dataset for this work.

To obtain robust and reliable galaxy morphologies, we applied the following stringent thresholding criteria (see Willett et al. 2017) to map the probability components in GZH to three categories (SPH, DISK, and IRR). The specific thresholds used are as follows:

1. SPH: $f_{\text{smooth, best}} > 0.70$, $f_{\text{features, best}} < 0.30$, and $f_{\text{round}} > 0.50$;
2. DISK: $f_{\text{features, best}} > 0.23$, $f_{\text{clumpy, no}} > 0.30$, $f_{\text{edge-on, no}} > 0.25$, $f_{\text{spiral}} > 0.25$, $f_{\text{odd, yes}} < 0.30$, and $f_{\text{irregular}} < 0.30$;
3. IRR: ($f_{\text{features, best}} > 0.23$, $f_{\text{clumpy, yes}} > 0.80$, $f_{\text{clump, asym}} > 0.50$) or ($f_{\text{odd, yes}} > 0.50$, and $f_{\text{irregular}} > 0.50$).

By cross-matching our sample with a curated morphological catalog, we ultimately obtained 757 galaxies with stable mor-

phologies for subsequent comparison. During this process, the UNC category was excluded as its proportion fell below 1% after matching.

Using the GZH catalog as a reference, we first compared the direct classification results of the two schemes. The overall consistency rate was 58%, indicating that although both methods captured similar global trends, notable discrepancies persisted near the morphological boundaries. To further investigate these differences, we performed a visual analysis in the feature space, adopting the t-SNE algorithm (van der Maaten & Hinton 2008) because it is more effective than UMAP at preserving local neighborhood structures in small samples (fewer than 1,000 galaxies). The features were derived from the ConvNeXt model and included both the original 2048-dimensional representations extracted directly from galaxy images and the 300-dimensional representations obtained via UMAP dimensionality reduction. By employing this dual-feature strategy, both sets of galaxy labels were projected

into the same feature space derived from the original image representations, ensuring a fairer comparison.

As shown in Figure 7, both in the original 2048-dimensional feature space and the reduced 300-dimensional space, our unsupervised classification results exhibit tighter intra-cluster distributions and clearer inter-cluster separation in the projection space. Compared to the distributions obtained through GZH probability label mapping, our approach demonstrates higher consistency and improved separability.

4.3. Validation with Galaxy Morphology and Structure Parameters

Since UMAP visualization only provides qualitative insights, we will conduct quantitative validation of the classification results by analyzing the distributions of multiple morphological parameters in this section. In general, parametric and nonparametric structural parameters serve as fundamental methods for characterizing their morphological classifications, so that galaxies with different morphologies typically exhibit specific distribution patterns in parameter space (e.g., Zhou et al. 2022; Dai et al. 2023; Yao et al. 2023; Song et al. 2024).

Due to the poorly understood evolutionary mechanisms of low-mass galaxies and to ensure the accuracy and reliability of physical parameter measurements, our analysis focuses exclusively on massive galaxies with stellar masses exceeding $10^9 M_{\odot}$. Out of the 50,056 successfully classified galaxies, 21,475 (42.9%) galaxies have stellar masses below this threshold and are therefore excluded, while 24,380 (48.7%) massive galaxies (after removing UNC-type) are retained for subsequent analysis in this subsection. We exclude UNC-type galaxies because their morphological parameters are difficult to measure, primarily constrained by relatively weak S/N.

4.3.1. Parametric Measurements

To obtain the morphological parameters of galaxies, we use the GALFIT package (Peng et al. 2002) and the GALAPAGOS software (Barden et al. 2012; Häußler et al. 2022) to fit the surface brightness profiles of galaxies with a single Sérsic model. We derive the Sérsic index n and effective radius r_e ¹ for each galaxy.

In Figure 8, panel (a) shows the distribution of Sérsic indices for the four galaxy types, with the median values for SPHs, ETDs, LTDs, and IRRs being 4.06, 1.81, 1.10, and 0.74, respectively. In general, SPHs tend to have higher n values due to their more concentrated light profiles, while IRRs typically have lower n values because of their more diffuse light distributions. As the light concentration decreases, the n values show a decreasing trend from SPHs to IRRs. Panel (b) illustrates the distribution of effective radii for the four galaxy types, with median r_e values of 1.86, 2.24, 3.71, and 4.47 kpc for SPHs, ETDs, LTDs, and IRRs, respectively. Typically, SPHs are more compact in structure and thus have smaller r_e , while IRRs are more diffuse and exhibit larger r_e values. As the spatial extension increases, r_e shows an increasing trend

from SPHs to IRRs. In short, the trends in Sérsic index and effective radius across different galaxy types are consistent with our expectations regarding their correlations.

4.3.2. Nonparametric Measurements

High-redshift galaxies exhibit irregular morphological structures, posing significant challenges in fitting their brightness profiles with empirical functions. In contrast, non-parametric morphological measurements require no presumptive light distribution models and can effectively capture structural characteristics of galaxies, making them widely applicable in evolutionary studies of high-redshift galaxies (Ferreira et al. 2023; Treu et al. 2023).

The most widely used nonparametric morphological indicators are the CAS statistics (Conselice et al. 2000; Conselice 2003), which include three parameters: concentration (C), asymmetry (A), and smoothness (S). Another widely adopted set of nonparametric morphological indicators is the G - M_{20} (Gini-moments20; Lotz et al. 2004, 2006) classification system. These parameters can be measured without requiring predefined galaxy center positions, making them particularly advantageous for studying high-redshift irregular galaxies and merging systems. Recently, Freeman et al. (2013) introduced the MID statistic, comprising three components: multimode (M), intensity (I), and deviation (D). We employ the `statmorph.csst` (Yao et al. 2023) package to measure these parameters. Additionally, we have incorporated extended optional morphological parameters as supplementary indicators, including Ψ (Law et al. 2007) and G_2 (Rosa et al. 2018). Given the widespread application of these parameters in numerous studies, detailed definitions and computational methodologies can be found in the corresponding references.

From the raincloud plot in Figure 9, we analyze the trends of the G and M_{20} parameters for different types of galaxies. Specifically, the G coefficients of galaxies show a gradual decrease from SPHs to IRRs, with median values of 0.57, 0.52, 0.49, and 0.47, respectively. Conversely, the M_{20} values of galaxies exhibit a gradual increase, with median values of -2.08, -1.79, -1.55, and -1.19, respectively. SPHs typically display the highest Gini coefficients and the lowest M_{20} values, whereas IRRs show the opposite characteristics. The observed trend from IRRs to SPHs in the figure aligns with our expectations (e.g., Zhou et al. 2022; Fang et al. 2023; Dai et al. 2023; Song et al. 2024).

In Figure 10, we show the distribution of the C and G_2 parameters for different types of galaxies. The parameter C (Conselice et al. 2000; Conselice 2003) is used to describe the concentration of a galaxy's light, with higher C values indicating a more compact light distribution. On the other hand, the G_2 parameter (Rosa et al. 2018) reflects the symmetry of gradient vectors in a galaxy's image. Higher G_2 values indicate stronger gradient asymmetry, which is common in spiral galaxies, while lower G_2 values are typically associated with elliptical galaxies, implying a more symmetric light distribution. In summary, spiral (elliptical) galaxies usually have G_2 values greater (less) than 1. The median values of the C parameter for each galaxy type gradually decrease to

¹ Defined as the radius enclosing half of the galaxy's total luminosity.

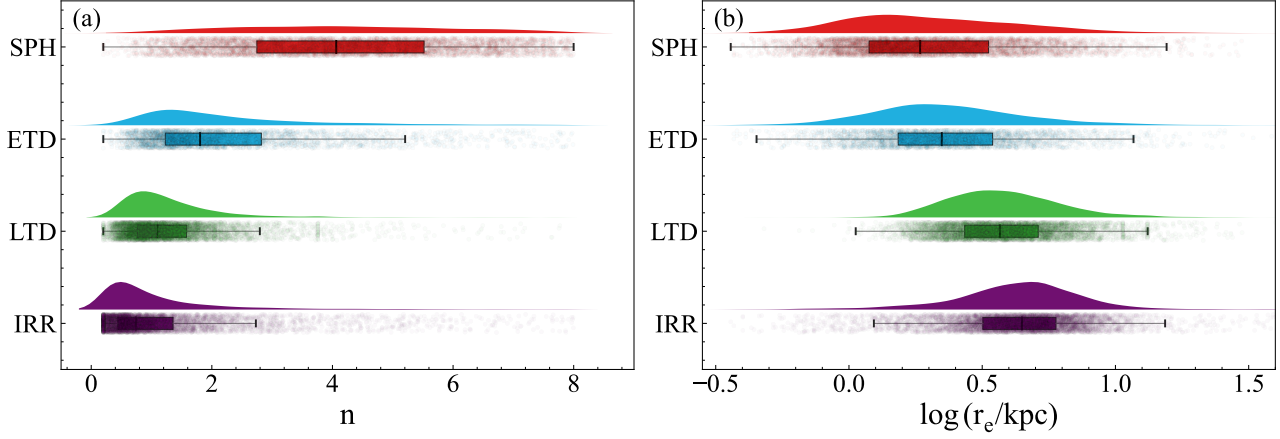


Figure 8. Raincloud plots of the Sérsic index (left panel) versus effective radius (right panel) for different massive galaxy types. The “cloud” portion of the plot reflects the data density distribution characteristics, and the “rain” plot portion demonstrates the degree of dispersion of the sample values. In the box plot, the lower boundary corresponds to the first quartile, the upper boundary corresponds to the third quartile, the horizontal line in the center indicates the median, and the upper and lower whisker ends of the box represent the maximum and minimum values. It can be seen that the Sérsic index gradually decreases as the galaxy type goes from SPHs to IRRs, while the effective radius gradually increases.

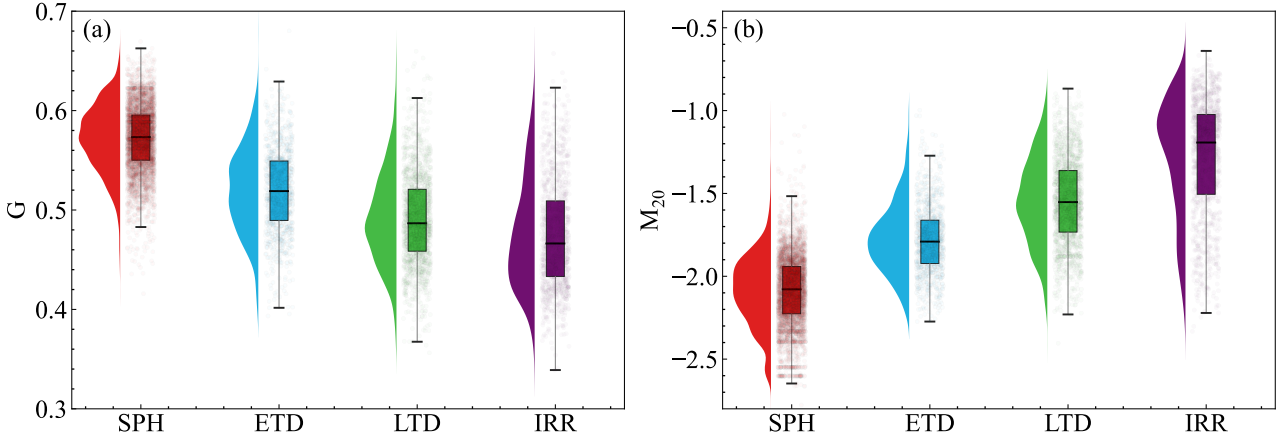


Figure 9. Raincloud plots of G (left panel) and M_{20} (right panel) for different types of massive galaxies. Analogues are similar to Figure 8. It can be seen that from SPHs to IRRs, the G of galaxies gradually decreases, while the M_{20} gradually increases.

3.59, 3.00, 2.75, and 2.54 as we move from SPHs to IRRs, respectively. The median values of G_2 gradually increase from SPHs to IRRs to 0.47, 1.53, 1.73, and 1.81, respectively. More compact galaxies tend to exhibit higher C and G_2 values, whereas those with higher asymmetry display the opposite. Our classification outcomes align with the observed patterns of variation.

The MID parameter can be used to measure the irregularity of galaxy morphology (Freeman et al. 2013). The larger the MID value, the more irregular the galaxy’s morphology. Conversely, more symmetric galaxies tend to have smaller MID values. As illustrated in Figure 11, the relatively compact and symmetric SPHs and IRRs exhibit smaller MID values, whereas the more diffuse and irregular LTD and IRR galaxies show larger MID values. The Ψ parameter describes the clumpy structures in a galaxy’s light distribution (Law et al. 2007). From SPHs to IRRs, galaxy concentration decreases,

and clumpy structures become more prominent. This observation validates the accuracy of our classification.

4.3.3. Quantitative Validation of Structural Consistency

To quantitatively evaluate the reliability of the unsupervised classification results in this study, we reclassified the four morphological classifications (SPH, ETD, LTD, and IRR) obtained by machine learning algorithms into two traditional morphological categories: Early-Type Galaxies (ETGs, synonymous with the SPH class) and Late-Type Galaxies (LTGs, encompassing ETD, LTD, and IRR classes). For cross-validation, we utilized two independent structural diagnostic approaches: one based on the Sérsic index and the other employing the G – M_{20} relationship.

The model-based criterion focuses on the Sérsic index, using the empirical threshold of $n = 2.5$ (van der Wel et al. 2008) as the dividing line between galaxies dominated by a

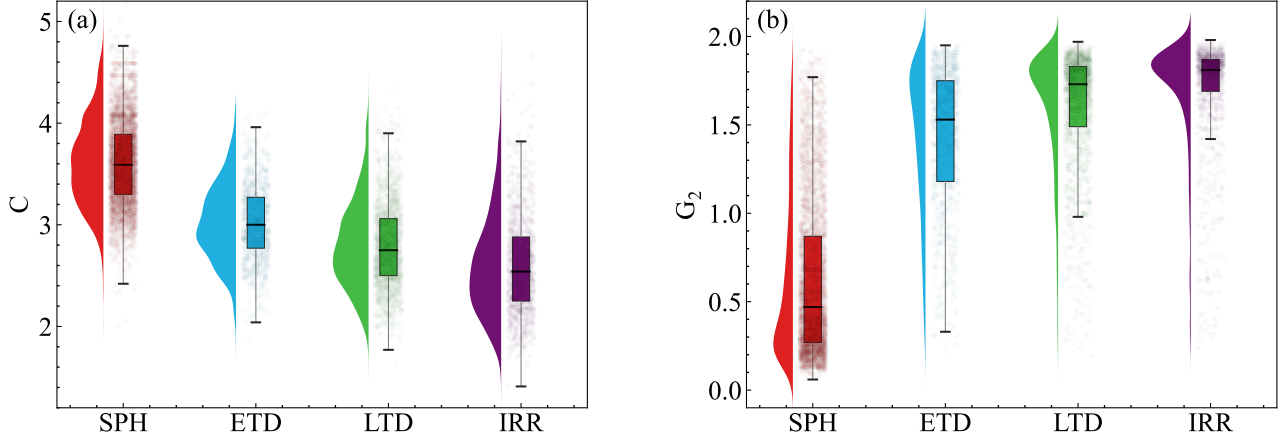


Figure 10. Raincloud plots of C (left panel) and G_2 (right panel) for different types of massive galaxies. Analogues are similar to Figure 8. It can be seen that from SPHs to IRRs, the C of galaxies gradually decreases, while the effective G_2 gradually increases.

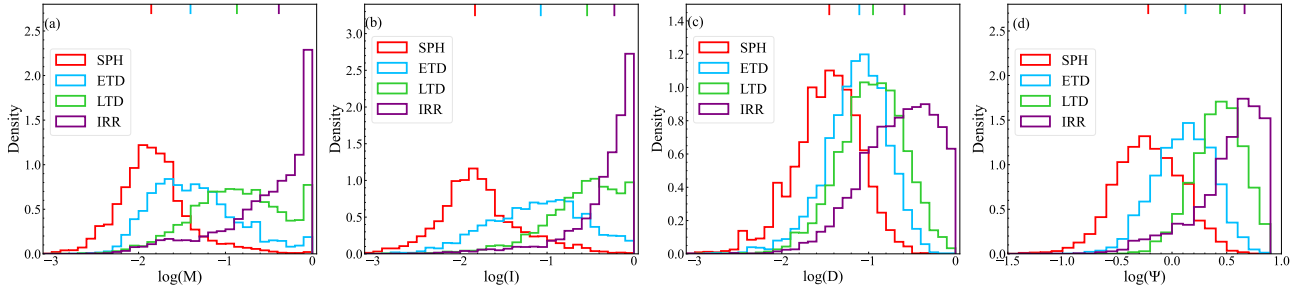


Figure 11. Distributions of Multimode (M , panel a), Intensity (I , panel b), and Deviation (D , panel c), and multiplicity (Ψ , panel d) for different types of massive galaxies. The top bars represent the median values of M , I , D , and Ψ for different types of galaxies. The median values of the galaxies are gradually increasing from SPHs to IRRs.

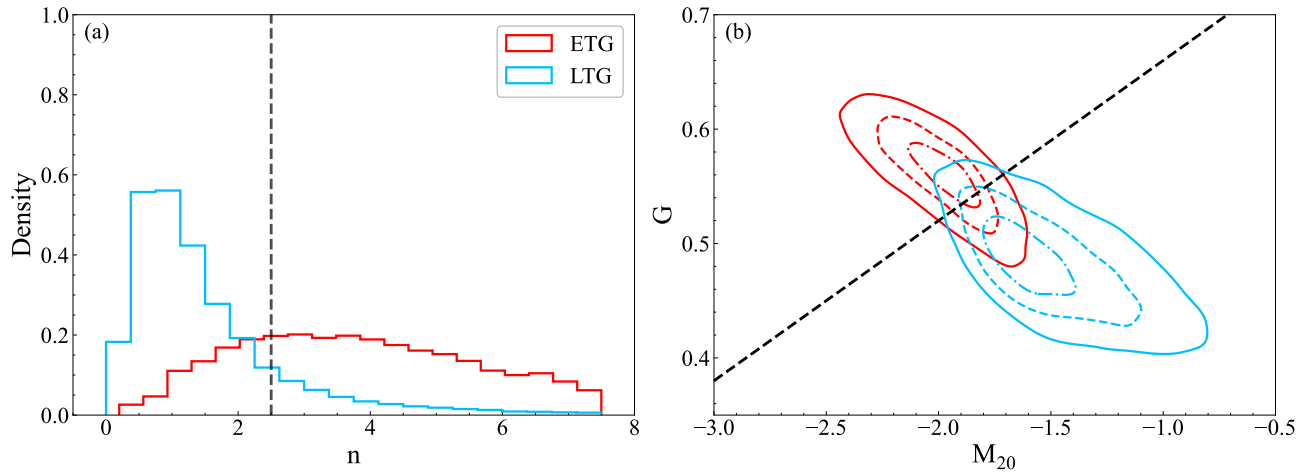


Figure 12. The panel (a) displays the distributions of the Sérsic index for early-type galaxies (ETGs) and late-type galaxies (LTGs). The gray dashed line marks the classification threshold at $n = 2.5$. The panel (b) shows the distribution in the $G - M_{20}$ plane for galaxies classified as ETGs and LTGs. The contour levels enclose 20%, 50%, and 80% of the respective subclass, from the innermost to the outermost regions. The dashed line, given by $G = 0.14M_{20} + 0.80$ (Lotz et al. 2008), represents the boundary between LTGs and ETGs.

bulge and those dominated by a disk. In contrast, the non-model-based approach employs the G – M_{20} classification proposed by Lotz et al. (2008). As depicted in Figure 12 (a), the distributions of ETGs and LTGs in Sérsic index space show a clear distinction: ETGs with median $n = 4.29$ are primarily found in the region where $n > 2.5$, while LTGs with median $n = 1.18$ predominantly reside in the region where $n < 2.5$. Utilizing $n = 2.5$ as the demarcation, we calculate the ETG probability when $n \geq 2.5$, $P(n \geq 2.5 | \text{ETG})$, and the LTG probability when $n < 2.5$, $P(n < 2.5 | \text{LTG})$:

$$P(n \geq 2.5 | \text{ETG}) = 83\%,$$

$$P(n < 2.5 | \text{LTG}) = 85\%.$$

These high probabilities indicate a high level of consistency between the machine learning labels and the classical classification based on luminosity profile morphology within the model-based parameter space. As expected, a larger Sérsic index corresponds to a luminosity distribution more concentrated towards the center, characteristic of bulge-dominated structures, while a smaller Sérsic index reflects galaxy systems where disk components are dominant.

Figure 12 (b) displays the two-dimensional G – M_{20} criterion as defined by Lotz et al. (2008). The ETG sample is predominantly positioned above the empirical dividing line, characterized by high G and low M_{20} values. Conversely, the LTG sample is mainly found below this line, featuring low G and high M_{20} values. To quantify the dominance of ETGs and LTGs in the individual $G - M_{20}$ regions to which they belong, we compute the probability of ETGs above the empirical line, $P(G_{\text{high}}, M_{20_{\text{low}}} | \text{ETG})$, and that of LTGs below the empirical line, $P((G_{\text{low}}, M_{20_{\text{high}}}) | \text{LTG})$:

$$P(G_{\text{high}}, M_{20_{\text{low}}} | \text{ETG}) = 74\%;$$

$$P(G_{\text{low}}, M_{20_{\text{high}}} | \text{LTG}) = 92\%.$$

The overall completeness rates of the two diagnostic methods are both above 84%, indicating that the unsupervised morphological classification results are statistically robust, and the resulting classification is consistent with the physical characteristics of the galaxies’ luminosity structures.

4.4. Evaluation of Catalog Completeness and Scientific Applicability

To assess the scientific reliability and applicability of the morphological catalog presented in this study, we employed a bagging clustering approach that integrates multiple clustering algorithms. Although this strategy reduced the successfully classified sample size (leaving $\sim 49\%$ of galaxies rejected), our strict voting mechanism reliably identified a set of galaxies with stable morphologies and high cross-algorithm classification consistency.

To evaluate the catalog’s reliability, we analyzed the completeness of the classified sample. Due to their low signal-to-noise ratios (S/Ns) and ambiguous morphological classifica-

tions, UNC-type galaxies were excluded from the analysis². The resulting high-confidence sample constitutes 42% of the total. For this sample, we computed completeness curves as a function of various physical and structural parameters, as shown in Figure 13. The results indicate that the classification completeness strongly depends on stellar mass, magnitude, signal-to-noise ratio, and certain morphological parameters (such as Sérsic index n , Gini coefficient G , and M_{20}), while being largely independent of redshift (z) and effective radius (r_e). Completeness is significantly higher for galaxies with higher S/Ns, brighter magnitudes, and more concentrated structures (i.e., higher n and G , lower M_{20}). This demonstrates that the bagging-based clustering approach is effective in identifying galaxies with higher resolution and clearer morphological features.

Figure 14 shows the distributions of successfully classified (51%) and rejected (49%) samples across key physical and structural parameters. To quantify the differences between these two groups, we performed Kolmogorov–Smirnov (K–S; Kolmogorov 1933) tests and effect size analyses. The K–S statistic reflects the overall difference between the distributions, Cohen’s d (Cohen 1988) measures the standardized difference between the means, and Cliff’s δ (Cliff 1993) evaluates the probability of superiority between the groups. For all parameters, the K–S test yields p -values below 0.05, while all effect sizes are small (with $|d| < 0.1$ and $|\delta| < 0.1$), indicating that although the differences are statistically significant, the actual discrepancies between successfully classified and rejected samples are minimal.

Notably, the remaining $\sim 49\%$ of rejected galaxies are retained in the catalog for future analysis and expansion. The currently constructed high-confidence sample can serve as a high-quality training set for supervised, semi-supervised, or transfer learning models, thereby enabling the extension of morphological labels to the entire galaxy population. Additionally, potential differences in parameter distributions between this high-quality training set and the broader target population do not significantly hinder the generalization of morphological learning. As demonstrated in previous studies (e.g., Domínguez Sánchez et al. 2019; Walmsley 2021; Song et al. 2024), models trained on well-defined subsets can be effectively fine-tuned or transferred to noisier and more complex datasets without introducing systematic biases.

5. SUMMARY

In this work, we improve the initial USmorph framework by introducing a pre-trained ConvNeXt model for feature encoding and combining it with the UMAP dimensionality reduction technique. By optimizing image feature extraction and dimensionality reduction processes, we reduce the number of categories for machine classification from 50 to 20 and save clustering time to one-fifth of the original, sig-

² The UNC quasar class is retained and can be used for tasks such as SML to identify galaxies with low S/Ns.

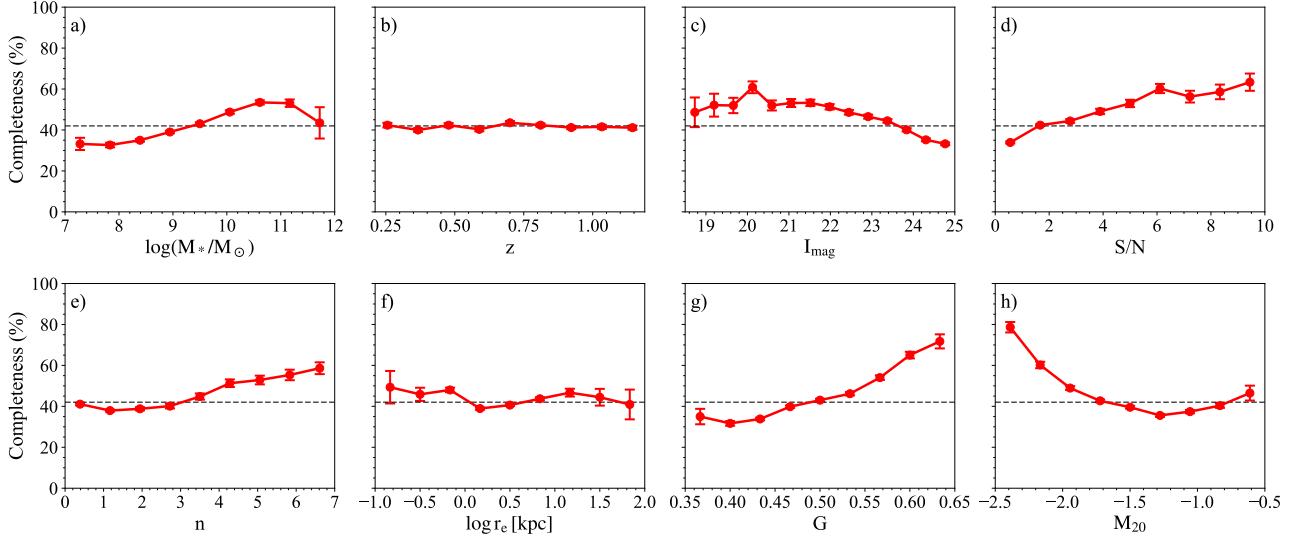


Figure 13. The completeness of the classified sample along various properties, including stellar mass, redshift, magnitude, average signal-to-noise ratio (S/N) per pixel, Sérsic index, effective radius (r_e), Gini coefficient (G), and M_{20} . Completeness is defined as the fraction of high-confidence samples within each parameter bin, with error bars indicating the 95% confidence interval.

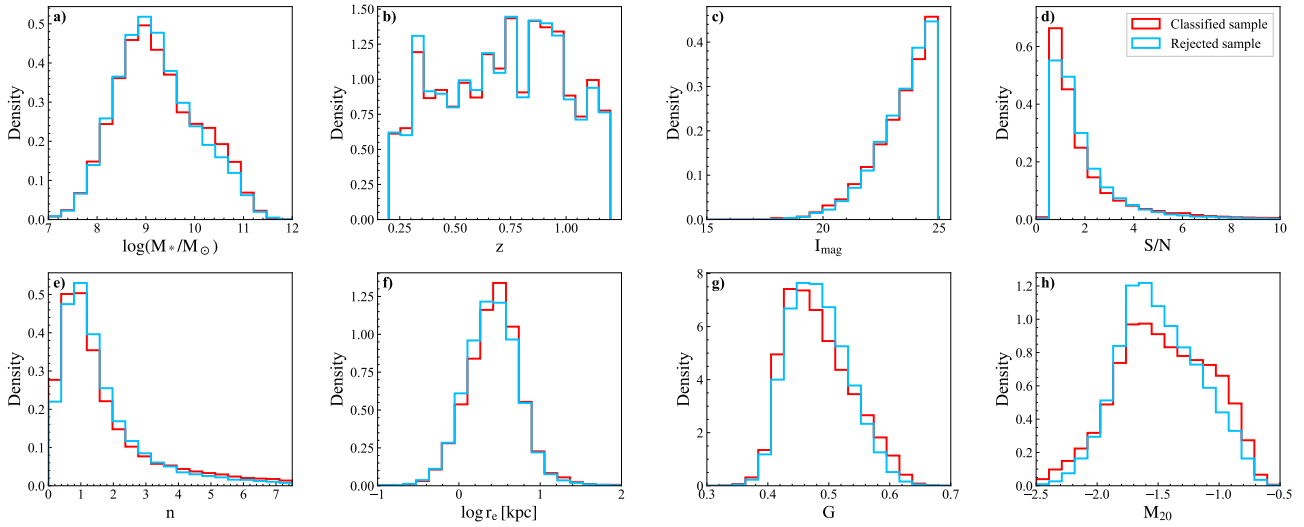


Figure 14. The distribution of Classified sample (red) and rejected sample (blue) across various physical and structural parameters.

nificantly decreasing computational resource consumption and enhancing classification visualization efficiency. The improved framework comprises the following four main steps:

- Pre-processing original images using CAE and APCT techniques to reduce noise and enhance rotational invariance.
- Encoding and extracting features from pre-processed data via a pre-trained ConvNeXt model, followed by UMAP dimensionality reduction to further reduce feature dimensions.
- Categorizing galaxies into 20 groups using a Bagging-based clustering model.

After visual inspection and removal of sources with inconsistent votes, 51% (50,056) of galaxies were successfully classified. The visual inspection was then combined to classify 50,056 sources in the COSMOS field into five categories: SPHs, ETDs, LTDs, IRRs, and UNC. In addition, classification reliability was validated through UMAP visualization analysis and galaxy physical parameter tests. The classification validity is further substantiated by significant differences in appearance characteristics and physical parameters among galaxy types.

Next-generation large-scale sky surveys, including the Legacy Survey of Space and Time at Rubin Observatory and those executed or planned by Euclid, the forthcoming CSST, and the Roman Space Telescope, will produce vast quantities of high-resolution, multi-band images. This neces-

sitates more efficient and adaptable data processing methods. Traditional supervised learning, dependent on annotated data, often experiences reduced recognition accuracy due to domain shift across different sky regions, telescopes, or bands. Our enhanced `USmorph` algorithm, integrating a ConvNeXt encoder with UMAP dimensionality reduction, significantly cuts computational costs and time for large-scale datasets. Unlike conventional methods, it utilizes pre-trained large models for feature extraction from any dataset, unaffected by variations in observation regions, equipment, or bands. This approach not only maintains high accuracy but also greatly improves the efficiency and adaptability of feature extraction, ideal for automated processing of cross-survey data.

Future work will focus on developing efficient large-model encoding methods and advanced dimensionality reduction techniques to boost machine learning accuracy. Additionally, we aim to explore features of special objects (e.g., tidal tails, gravitational lenses, and little red dots) via subclass subdivision and optimize the algorithm into an intuitive, user-friendly

software tool to support efficient technical deployment for survey telescopes on the Chinese space station.

This work is supported by the National Natural Science Foundation of China (NSFC) (grant Nos. 12233008 and 12573012, and Project No. 12503011), the National Key R&D Program of China (grant No. 2023YFA1608100), the Strategic Priority Research Program of the Chinese Academy of Sciences (grant No. XDB0550200), the Cyrus Chun Ying Tang Foundations, and the 111 Project for “Observational and Theoretical Research on Dark Matter and Dark Energy” (B23042), and the China Manned Space Program with grant No. CMS-CSST-2025-A04. S.L. acknowledges the support from the Key Laboratory of Modern Astronomy and Astrophysics (Nanjing University) by the Ministry of Education. The numerical calculations in this paper have been done on the platform of the High Performance Computing of Anqing Normal University.

REFERENCES

- Barden, M., Haussler, B., Peng, C. Y., McIntosh, D. H., & Guo, Y. 2012, *Monthly Notices of the Royal Astronomical Society*, 422, 449. <https://api.semanticscholar.org/CorpusID:119117461>
- Brammer, G. B., van Dokkum, P. G., & Coppi, P. 2008, *The Astrophysical Journal*, 686, 1503, doi: [10.1086/591786](https://doi.org/10.1086/591786)
- Chabrier, G. 2003, *Publications of the Astronomical Society of the Pacific*, 115, 763, doi: [10.1086/376392](https://doi.org/10.1086/376392)
- Chen, T., Kornblith, S., Norouzi, M., & Hinton, G. 2020, in *Proceedings of the 37th International Conference on Machine Learning, ICML'20 (JMLR.org)*
- Cheng, T.-Y., Huertas-Company, M., Conselice, C. J., et al. 2021, *Monthly Notices of the Royal Astronomical Society*, 503, 4446, doi: [10.1093/mnras/stab734](https://doi.org/10.1093/mnras/stab734)
- Cliff, N. 1993, *Psychological Bulletin*, 114, 494, doi: [10.1037/0033-2909.114.3.494](https://doi.org/10.1037/0033-2909.114.3.494)
- Cohen, J. 1988, *Statistical Power Analysis for the Behavioral Sciences*, 2nd edn. (New York: Routledge), doi: [10.4324/9780203771587](https://doi.org/10.4324/9780203771587)
- Conselice, C. J. 2003, *ApJS*, 147, 1, doi: [10.1086/375001](https://doi.org/10.1086/375001)
- Conselice, C. J., Bershad, M. A., & Jangren, A. 2000, *The Astrophysical Journal*, 529, 886, doi: [10.1086/308300](https://doi.org/10.1086/308300)
- Dai, Y., Xu, J., Song, J., et al. 2023, *The Astrophysical Journal Supplement Series*, 268, 34, doi: [10.3847/1538-4365/ace69e](https://doi.org/10.3847/1538-4365/ace69e)
- Davies, D. L., & Bouldin, D. W. 1979, *IEEE Transactions on Pattern Analysis and Machine Intelligence, PAMI-1*, 224, doi: [10.1109/TPAMI.1979.4766909](https://doi.org/10.1109/TPAMI.1979.4766909)
- Davis, D. R., & Hayes, W. B. 2014, *The Astrophysical Journal*, 790, 87, doi: [10.1088/0004-637X/790/2/87](https://doi.org/10.1088/0004-637X/790/2/87)
- Dieleman, S., Willett, K. W., & Dambre, J. 2015, *Monthly Notices of the Royal Astronomical Society*, 450, 1441–1459, doi: [10.1093/mnras/stv632](https://doi.org/10.1093/mnras/stv632)
- Domínguez Sánchez, H., Huertas-Company, M., Bernardi, M., et al. 2019, *MNRAS*, 484, 93, doi: [10.1093/mnras/sty3497](https://doi.org/10.1093/mnras/sty3497)
- Dosovitskiy, A., Beyer, L., Kolesnikov, A., et al. 2021, *An Image is Worth 16x16 Words: Transformers for Image Recognition at Scale*. <https://arxiv.org/abs/2010.11929>
- Fang, G., Ba, S., Gu, Y., et al. 2023, *The Astronomical Journal*, 165, 35, doi: [10.3847/1538-3881/aca1a6](https://doi.org/10.3847/1538-3881/aca1a6)
- Fernando, T., Rathnayake, S., & Dissanayaka, K. 2024, in *2024 6th International Conference on Advancements in Computing (ICAC)*, 229–234, doi: [10.1109/ICAC64487.2024.10851157](https://doi.org/10.1109/ICAC64487.2024.10851157)
- Ferreira, L., Conselice, C. J., Sazonova, E., et al. 2023, *ApJ*, 955, 94, doi: [10.3847/1538-4357/acec76](https://doi.org/10.3847/1538-4357/acec76)
- Flügge, S. 1959, *Handbuch der Physik*, 11, doi: [10.1007/978-3-642-45932-0](https://doi.org/10.1007/978-3-642-45932-0)
- Freeman, P. E., Izbicki, R., Lee, A. B., et al. 2013, *Monthly Notices of the Royal Astronomical Society*, 434, 282, doi: [10.1093/mnras/stt1016](https://doi.org/10.1093/mnras/stt1016)
- Ghosh, A., Urry, C. M., Powell, M. C., et al. 2024, *ApJ*, 971, 142, doi: [10.3847/1538-4357/ad596f](https://doi.org/10.3847/1538-4357/ad596f)
- Gong, S., Boddeti, V. N., & Jain, A. K. 2018, 2019 *IEEE/CVF Conference on Computer Vision and Pattern Recognition (CVPR)*, 3982. <https://api.semanticscholar.org/CorpusID:125095565>
- Grill, J.-B., Strub, F., Alth'e, F., et al. 2020, *ArXiv*, abs/2006.07733. <https://api.semanticscholar.org/CorpusID:219687798>
- Gui, J., Chen, T., Zhang, J., et al. 2024, *IEEE Trans. Pattern Anal. Mach. Intell.*, 46, 9052–9071, doi: [10.1109/TPAMI.2024.3415112](https://doi.org/10.1109/TPAMI.2024.3415112)
- Halkidi, M., Batistakis, Y., & Vazirgiannis, M. 2001, *Journal of Intelligent Information Systems*, 17, 107, doi: [10.1023/A:1012801612483](https://doi.org/10.1023/A:1012801612483)

- Hartigan, J. A., & Wong, M. A. 1979, *Journal of the Royal Statistical Society. Series C (Applied Statistics)*, 28, 100. <http://www.jstor.org/stable/2346830>
- Häußler, B., Vika, M., Bamford, S. P., et al. 2022, *A&A*, 664, A92, doi: [10.1051/0004-6361/202142935](https://doi.org/10.1051/0004-6361/202142935)
- He, K., Zhang, X., Ren, S., & Sun, J. 2015, *Deep Residual Learning for Image Recognition*. <https://arxiv.org/abs/1512.03385>
- Hubble, E. P. 1926, *ApJ*, 64, 321, doi: [10.1086/143018](https://doi.org/10.1086/143018)
- Huertas-Company, M., Gravet, R., Cabrera-Vives, G., et al. 2015, *The Astrophysical Journal Supplement Series*, 221, 8, doi: [10.1088/0067-0049/221/1/8](https://doi.org/10.1088/0067-0049/221/1/8)
- Huertas-Company, M., Iyer, K. G., Angeloudi, E., et al. 2024, *A&A*, 685, A48, doi: [10.1051/0004-6361/202346800](https://doi.org/10.1051/0004-6361/202346800)
- Ilbert, O., Capak, P., Salvato, M., et al. 2008, *The Astrophysical Journal*, 690, 1236, doi: [10.1088/0004-637X/690/2/1236](https://doi.org/10.1088/0004-637X/690/2/1236)
- Jang, H., & Tong, F. 2024, *Nature Communications*, 15, 1989, doi: [10.1038/s41467-024-45679-0](https://doi.org/10.1038/s41467-024-45679-0)
- Kauffmann, G., White, S. D. M., Heckman, T. M., et al. 2004, *Monthly Notices of the Royal Astronomical Society*, 353, 713, doi: [10.1111/j.1365-2966.2004.08117.x](https://doi.org/10.1111/j.1365-2966.2004.08117.x)
- Kawinwanichakij, L., Papovich, C., Quadri, R. F., et al. 2017, *The Astrophysical Journal*, 847, 134, doi: [10.3847/1538-4357/aa8b75](https://doi.org/10.3847/1538-4357/aa8b75)
- Koekemoer, A. M., Fruchter, A. S., Hook, R. N., & Hack, W. 2003, in *HST Calibration Workshop : Hubble after the Installation of the ACS and the NICMOS Cooling System*, 337
- Koekemoer, A. M., Aussel, H., Calzetti, D., et al. 2007, *The Astrophysical Journal Supplement Series*, 172, 196, doi: [10.1086/520086](https://doi.org/10.1086/520086)
- Kolesnikov, I., Sampaio, V. M., de Carvalho, R. R., et al. 2023, *Monthly Notices of the Royal Astronomical Society*, 528, 82, doi: [10.1093/mnras/stad3934](https://doi.org/10.1093/mnras/stad3934)
- Kolmogorov, A. N. 1933, *Giornale dell'Istituto Italiano degli Attuari*, 4, 83. <https://api.semanticscholar.org/CorpusID:222427298>
- Krizhevsky, A., Sutskever, I., & Hinton, G. E. 2012, *Communications of the ACM*, 60, 84. <https://api.semanticscholar.org/CorpusID:195908774>
- Lang, D., Hogg, D. W., & Mykytyn, D. 2016, *The Tractor: Probabilistic astronomical source detection and measurement*, *Astrophysics Source Code Library*, record ascl:1604.008. <https://ui.adsabs.harvard.edu/abs/2016ascl.soft04008L>
- Law, D. R., Steidel, C. C., Erb, D. K., et al. 2007, *The Astrophysical Journal*, 656, 1, doi: [10.1086/510357](https://doi.org/10.1086/510357)
- Lecun, Y., Bottou, L., Bengio, Y., & Haffner, P. 1998, *Proceedings of the IEEE*, 86, 2278, doi: [10.1109/5.726791](https://doi.org/10.1109/5.726791)
- Liu, Z., Mao, H., Wu, C.-Y., et al. 2022, in *2022 IEEE/CVF Conference on Computer Vision and Pattern Recognition (CVPR)*, 11966–11976, doi: [10.1109/CVPR52688.2022.01167](https://doi.org/10.1109/CVPR52688.2022.01167)
- Liu, Z., Zhang, F., Cheng, L., et al. 2023, *Simple But Effective Unsupervised Classification for Specified Domain Images: A Case Study on Fungi Images*, <https://ssrn.com/abstract=4673082>, doi: [10.2139/ssrn.4673082](https://doi.org/10.2139/ssrn.4673082)
- Lotz, J. M., Madau, P., Giavalisco, M., Primack, J., & Ferguson, H. C. 2006, *The Astrophysical Journal*, 636, 592, doi: [10.1086/497950](https://doi.org/10.1086/497950)
- Lotz, J. M., Primack, J., & Madau, P. 2004, *The Astronomical Journal*, 128, 163, doi: [10.1086/421849](https://doi.org/10.1086/421849)
- Lotz, J. M., Davis, M., Faber, S. M., et al. 2008, *ApJ*, 672, 177, doi: [10.1086/523659](https://doi.org/10.1086/523659)
- Lowe, S. C., Haurum, J. B., Oore, S., Moeslund, T. B., & Taylor, G. W. 2024, in *ICML 2024 Workshop on Foundation Models in the Wild*
- Mao, J., Griniasty, I., Teoh, H. K., et al. 2024, *Proceedings of the National Academy of Sciences*, 121, e2310002121, doi: [10.1073/pnas.2310002121](https://doi.org/10.1073/pnas.2310002121)
- Masci, J., Meier, U., Cireşan, D., & Schmidhuber, J. 2011, in *Artificial Neural Networks and Machine Learning – ICANN 2011*, ed. T. Honkela, W. Duch, M. Girolami, & S. Kaski (Berlin, Heidelberg: Springer Berlin Heidelberg), 52–59
- Maćkiewicz, A., & Ratajczak, W. 1993, *Computers & Geosciences*, 19, 303, doi: [https://doi.org/10.1016/0098-3004\(93\)90090-R](https://doi.org/10.1016/0098-3004(93)90090-R)
- McInnes, L., & Healy, J. 2018, *ArXiv*, abs/1802.03426. <https://api.semanticscholar.org/CorpusID:3641284>
- Murtagh, F. 1983, *The Computer Journal*, 26, 354, doi: [10.1093/comjnl/26.4.354](https://doi.org/10.1093/comjnl/26.4.354)
- Murtagh, F., & Legendre, P. 2014, *Journal of Classification*, 31, 274–295, doi: [10.1007/s00357-014-9161-z](https://doi.org/10.1007/s00357-014-9161-z)
- Oke, J. B., & Gunn, J. E. 1983, *ApJ*, 266, 713, doi: [10.1086/160817](https://doi.org/10.1086/160817)
- Omand, C. M. B., Balogh, M. L., & Poggianti, B. M. 2014, *Monthly Notices of the Royal Astronomical Society*, 440, 843, doi: [10.1093/mnras/stu331](https://doi.org/10.1093/mnras/stu331)
- Peng, C. Y., Ho, L. C., Impey, C. D., & Rix, H.-W. 2002, *The Astronomical Journal*, 124, 266, doi: [10.1086/340952](https://doi.org/10.1086/340952)
- Reyes, E., Estévez, P. A., Reyes, I., et al. 2018, in *2018 International Joint Conference on Neural Networks (IJCNN)*, 1–8, doi: [10.1109/IJCNN.2018.8489627](https://doi.org/10.1109/IJCNN.2018.8489627)
- Rosa, R. R., de Carvalho, R. R., Sautter, R. A., et al. 2018, *MNRAS*, 477, L101, doi: [10.1093/mnras/sly054](https://doi.org/10.1093/mnras/sly054)
- Russakovsky, O., Deng, J., Su, H., et al. 2015, *Int. J. Comput. Vision*, 115, 211–252, doi: [10.1007/s11263-015-0816-y](https://doi.org/10.1007/s11263-015-0816-y)
- Scoville, N., Aussel, H., Brusa, M., et al. 2007, *The Astrophysical Journal Supplement Series*, 172, 1–8, doi: [10.1086/516585](https://doi.org/10.1086/516585)
- Simmons, B. D., Melvin, T., Lintott, C., et al. 2014, *Monthly Notices of the Royal Astronomical Society*, 445, 3466, doi: [10.1093/mnras/stu1817](https://doi.org/10.1093/mnras/stu1817)
- Siudek, M., Małek, K., Pollo, A., et al. 2022, *A&A*, 666, A131, doi: [10.1051/0004-6361/202243613](https://doi.org/10.1051/0004-6361/202243613)

- Song, J., Fang, G., Ba, S., et al. 2024, *The Astrophysical Journal Supplement Series*, 272, 42, doi: [10.3847/1538-4365/ad434f](https://doi.org/10.3847/1538-4365/ad434f)
- Stoughton, C., Lupton, R. H., Bernardi, M., et al. 2002, *AJ*, 123, 485, doi: [10.1086/324741](https://doi.org/10.1086/324741)
- Su, Y., Fang, G., Lu, S., & Lin, Z. 2025, *A&A*, 699, A184, doi: [10.1051/0004-6361/202553693](https://doi.org/10.1051/0004-6361/202553693)
- Treu, T., Calabrò, A., Castellano, M., et al. 2023, *ApJL*, 942, L28, doi: [10.3847/2041-8213/ac9283](https://doi.org/10.3847/2041-8213/ac9283)
- van der Maaten, L., & Hinton, G. 2008, *Journal of Machine Learning Research*, 9, 2579
- van der Wel, A., Holden, B. P., Zirm, A. W., et al. 2008, *ApJ*, 688, 48, doi: [10.1086/592267](https://doi.org/10.1086/592267)
- Walmsley, M. 2021, in *American Astronomical Society Meeting Abstracts*, Vol. 238, American Astronomical Society Meeting Abstracts, 119.02
- Weaver, J. R., Kauffmann, O. B., Ilbert, O., et al. 2022, *The Astrophysical Journal Supplement Series*, 258, 11, doi: [10.3847/1538-4365/ac3078](https://doi.org/10.3847/1538-4365/ac3078)
- Willett, K. W., Galloway, M. A., Bamford, S. P., et al. 2017, *MNRAS*, 464, 4176, doi: [10.1093/mnras/stw2568](https://doi.org/10.1093/mnras/stw2568)
- Woo, S., Debnath, S., Hu, R., et al. 2023, in *2023 IEEE/CVF Conference on Computer Vision and Pattern Recognition (CVPR)*, 16133–16142, doi: [10.1109/CVPR52729.2023.01548](https://doi.org/10.1109/CVPR52729.2023.01548)
- Yao, X., Feng, X., Cheng, G., Han, J., & Guo, L. 2019, in *IGARSS 2019 - 2019 IEEE International Geoscience and Remote Sensing Symposium*, 1382–1385, doi: [10.1109/IGARSS.2019.8899285](https://doi.org/10.1109/IGARSS.2019.8899285)
- Yao, Y., Song, J., Kong, X., et al. 2023, *The Astrophysical Journal*, 954, 113, doi: [10.3847/1538-4357/ace7b5](https://doi.org/10.3847/1538-4357/ace7b5)
- York, D. G., Adelman, J., Anderson, Jr., J. E., et al. 2000, *The Astronomical Journal*, 120, 1579, doi: [10.1086/301513](https://doi.org/10.1086/301513)
- Zhang, T., Ramakrishnan, R., & Livny, M. 1996, *SIGMOD Rec.*, 25, 103–114, doi: [10.1145/235968.233324](https://doi.org/10.1145/235968.233324)
- Zhou, C., Gu, Y., Fang, G., & Lin, Z. 2022, *The Astronomical Journal*, 163, 86, doi: [10.3847/1538-3881/ac4245](https://doi.org/10.3847/1538-3881/ac4245)
- Zhu-Ge, J.-M., Luo, J.-W., & Zhang, B. 2023, *MNRAS*, 519, 1823, doi: [10.1093/mnras/stac3599](https://doi.org/10.1093/mnras/stac3599)
- Ćiprijanović, A., Lewis, A., Pedro, K., et al. 2023, *Machine Learning: Science and Technology*, 4, 025013, doi: [10.1088/2632-2153/acca5f](https://doi.org/10.1088/2632-2153/acca5f)